International Journal of Rock Mechanics & Mining Sciences 180 (2024) 105819

Contents lists available at ScienceDirect

International Journal of Rock Mechanics and Mining Sciences

journal homepage: www.elsevier.com/locate/ijrmms

Roles of heat and stress transfer in triggering fault instability in conjugate faulted reservoirs

Yueqiang Ma [a,b], Kaiwen Xia [c], Qinghua Lei [d,e], Chongyuan Zhang [f,g], Derek Elsworth [h], Quan Gan [a,b,*], Liang Yuan [i,j,**]

[a] State Key Laboratory of Coal Mine Disaster Dynamics and Control, Chongqing, China
[b] School of Resources and Safety Engineering, Chongqing University, Chongqing, China
[c] Institute of Geosafety, School of Engineering and Technology, China University of Geosciences (Beijing), Beijing, China
[d] Department of Earth Sciences, Uppsala University, Sweden
[e] Department of Earth Sciences, ETH, Zurich, Switzerland
[f] Institute of Geomechanics, Chinese Academy of Geological Sciences, Beijing, 100081, China
[g] School of Mechanics and Civil Engineering, China University of Mining and Technology, Beijing 100083, China
[h] Department of Energy and Mineral Engineering, EMS Energy Institute and G3 Center, Pennsylvania State University, University Park, PA, USA
[i] Beijing Key Laboratory for Precise Mining of Intergrown Energy and Resources, China University of Mining and Technology (Beijing), Beijing, China
[j] Joint National-Local Engineering Research Center for Safe and Precise Coal Mining, Anhui University of Science & Technology, Huainan, China

ARTICLE INFO

Keywords:
Induced fault instability
Stress transfer
Thermal stress
THM

ABSTRACT

The presence of multiple conjugate but non-intersecting faults in geothermal reservoirs presents issues related to fault interaction in the presence of complex coupled thermo-hydro-mechanical (THM) processes in influencing the triggering of seismicity. We examine alternate strategies in stimulating such a conjugate-faulted geothermal reservoir analogous to that hosting the M_w 5.5 Pohang earthquake (2017). We evaluate the response of the reservoir to both short-term stimulation (1y) and long-term production (10y), both with and without thermal effects – for a large fault (F1) adjacent to a non-intersecting smaller fault (F2) and in a reverse faulting stress regime. Results suggest that the slip on either fault impacts the stress state on the other fault through stress transfer. Reactivation of the minor fault (F2) transfers stress towards to the upper part of primary fault (F1), inducing instability. The slip of the major fault is delayed by positioning the location of injection away from the junction between the two faults – decreasing the injection depth from 4087.5 m to 3712.5 m delays the time to slip by 2.61 y. Furthermore, thermal stress plays a decisive role in prompting late-stage fault reactivation for long-term fluid circulation where pore pressures have already reached steady state. The pattern of thermal unloading follows the path of fluid transport and heat transfer along the faults. Overall, this study not only advances our understanding of mechanisms of injection-induced fault instability in EGS reservoirs with multiple and closely-interacting faults, but also provides insights into how different injection strategies can delay or mitigate induced seismicity.

1. Introduction

Geothermal energy, as a promising means to address the energy crisis and reduce greenhouse gas emissions from the burning of fossil fuels, has attracted widespread attention worldwide.[1,2] Enhanced geothermal systems (EGSs), which extract heat from hot basement rock at great depths with originally ultralow permeabilities and high temperatures by creating fracture networks through hydraulic stimulation, have great potential to produce baseload electrical power.[3] However, induced seismicity caused by fluid injection has resulted in several EGS projects being delayed or canceled, raising widespread concern regarding the feasibility of this technology.[4] Although the magnitudes of induced earthquakes have generally been relatively small,[5,6] some have been large, causing significant damage to property and economic losses.[7] For

* Corresponding author. State Key Laboratory of Coal Mine Disaster Dynamics and Control, Chongqing, China.
** Corresponding author. Beijing Key Laboratory for Precise Mining of Intergrown Energy and Resources, China University of Mining and Technology (Beijing), Beijing, China.
E-mail addresses: quan.gan@cqu.edu.cn (Q. Gan), yuanl_1960@sina.com (L. Yuan).

https://doi.org/10.1016/j.ijrmms.2024.105819
Received 12 September 2023; Received in revised form 9 June 2024; Accepted 22 June 2024

example, a M_w 4.6 event occurred at the Geysers geothermal site in the US in 1982,[8] a M_w 3.7 event at the Cooper Basin geothermal site in Australia in 2003,[4] an M_L 3.4 event at the Basel EGS in Switzerland in 2006,[9] and a M_w 5.5 event occurred at the Pohang geothermal site in South Korea in November 2017.[10] In view of the significant societal and economic impact, studying the mechanisms of injection-induced seismicity to better understand and mitigate the occurrence of large induced earthquakes is of great importance.

Fluid injection-induced seismicity has occurred in many underground engineering projects, including wastewater disposal,[11] carbon dioxide sequestration,[12] and enhanced oil and gas recovery.[13,14] Mechanisms contributing to this injection-induced seismicity have been investigated based on laboratory experiments,[15] field tests,[16] and numerical models. Most large-magnitude induced earthquakes are correlated with the presence of pre-existing faults and an ambient critical stress state.[17] Also, pore pressure diffusion plays an essential role in the fault reactivation[18]; the fluid pressure increase due to fluid injection reduces the effective normal stress, leading to a reduction in shear strength. Another mechanism inducing seismic reactivation is related to poroelastic stressing.[19] Different from direct fluid pressurization, deformation of the surrounding reservoir may spread to the far field *via* stress transfer – potentially destabilizing distant faults without direct fluid communication.[20] Furthermore, thermal drawdown caused by cold-water injection may trigger fault reactivation.[21–24] Fluid-induced aseismic events[25,26] and small earthquakes[15,27] can also transfer Coulomb static stress and further trigger seismicity. Other possible mechanisms for triggering fault activation include cooling,[28] earthquake interaction,[29] geochemical/mineralogical alteration,[30] and thermal pressurization.[31]

Currently, the most prominent example of an induced earthquake in a geothermal reservoir is the magnitude M_w 5.5 seismic event close to the Pohang geothermal site in Korea, on November 15, 2017.[32] Two wells (PX-1 and PX-2) were drilled into the granitic basement to a depth of 4215 m and 4348 m, respectively, from 2012 to 2016. A total of five hydraulic stimulations were carried out alternately in PX-1 and PX-2 from January 29, 2016 to September 18, 2017, leading to a M_w 3.2 event on April 15, 2017 during the stimulation period and a M_w 5.5 mainshock two months after the stimulation period.[33] The mainshock caused numerous injuries and more than US$300 million in total economic loss.[33]

Significant effort has been made for a better understanding of the hydraulic and geomechanical processes occurring in hydraulic stimulation, particularly in relation to the Pohang geothermal project.[34] Seismological and geodetic analyses have suggested a causal connection between EGS development and the M_w 5.5 earthquake in Pohang.[35] By analyzing geological, geophysical, and reservoir stimulation data, the temporal relationship between seismicity and fluid injection, as well as the spatial relationship between the hypocenters and the EGS site, have indicated that the Pohang earthquake was induced.[7] Earthquakes that have occurred around the EGS site over the past 10 years have been collected and analyzed, providing evidence for the hypothesis that the earthquake was triggered by fluid injection to a critically stressed fault.[34] More detailed hydromechanical modeling and analysis of the first and second hydraulic stimulations in wells PX-1 and PX-2 have been conducted to improve the understanding of the hydro-mechanical and induced seismic characteristics.[36–38] These studies considered the presence of fractures intersecting the open-hole sections of the wells and found that immediate stress transfer and delayed fluid migration played a significant role in understanding seismic response of the M_w 5.5 fault.[39] Field-scale simulations with variation in well design have been applied to advance physical understanding of how different configurations of well operations can mitigate the potential for induced seismicity.[40] The maximum induced earthquake magnitude (M_{max}) has been found to scale with the logarithm of the elapsed time from the beginning of the fluid injection to the occurrence of the earthquake, which is also the case for the Pohang Earthquake.[41] Additionally, the geochemistry of the water that flows back from the geothermal stimulation has been analyzed, indicating that fault corrosion may be a potential cause of the M_w 5.5 earthquake.[30,42,43]

The above details describing the M_w 5.5 Pohang earthquake attempt to reveal the possible mechanisms of the earthquake from different aspects, such as pore pressure increase, poroelastic stress changes, and fault weakening caused by water-rock interactions. However, they do not consider the scenario in which multiple conjugate but non-intersecting faults exist in geothermal reservoirs. Under these circumstances, fault interaction with complex THM processes influences the stability of adjacent faults. The reactivation of one fault caused by fluid injection leads to deformation in the reservoir rock, redistributing stress and potentially promoting the slip of the adjacent fault. However, the role of stress transfer in fault instability in conjugate faulted reservoirs needs further study. Multiple observations at Pohang confirm the existence of an inclined fault between PX-1 and PX-2, and the relocation of seismic activity has also identified a smaller fault near PX-1.[33] The smaller fault has been accommodated in some analyses.[44] Here, the perturbation in pore pressure triggers seismicity on critically stressed faults, and those earthquake interactions trigger successive events. However, that work did not consider the influence of thermal stress caused by cold water injection.

Due to the relevance and data availability of the Pohang geothermal site, we utilize data from this particular site to develop our model. Our study aims to investigate the hydraulic, heat transfer, and stress transfer effects caused by cold fluid injection on triggering fault instability. The data from the Pohang site provide a concrete example to base our simulations on, ensuring that the model parameters are realistic and relevant. This approach allows us to explore general principles and mechanisms that could apply to similar geothermal sites.

We develop a pseudo 3D model using the TOUGH-FLAC3D simulator[45] to model coupled thermo-hydro-mechanical processes in an EGS reservoir subject to fluid injection and circulation. This coupled THM computational platform has been validated and extensively applied to study the problem of fault instability in the context of EGS reservoirs.[21,22,46–48] We aim to develop an improved conceptual understanding of how stress transfer influences fault stability in the presence of a non-intersecting conjugate fault set. We study the thermal effect caused by cold fluid injection on fault stability by comparing the timing and magnitude of earthquakes induced by fluid injection, both with and without considering thermal effect. Finally, simulations with different injection strategies are conducted to advance our understanding of how different injection strategies can relieve or delay the induced seismicity. Although the work reported here is placed in the context of the Pohang EGS project, we emphasize that our goal is not to derive a fully calibrated and validated model of the Pohang EGS, but to provide insights applicable to similar fault geometries.

2. Modeling approach

2.1. Simulator introduction

TOUGH-FLAC3D is an undrained, modular THM simulator that couples the thermal and hydraulic capabilities of TOUGH with the mechanical calculations of FLAC3D. We use the EOS1 module, which provides a description of pure water in the liquid, vapor, and two-phase states. The coupling procedure is illustrated in Fig. 1. The coupling in TOUGH-FLAC3D is two-way. The simulation begins with the equilibration of temperature and pore pressure in TOUGH . The TOUGH central node data are then interpolated to corner node information to serve as input for FLAC3D. After reaching a stress equilibrium state in FLAC3D, the pressure response is obtained. The effective stress is then used to determine the permeability change. Parameters are subsequently re-entered into TOUGH for the next time step.

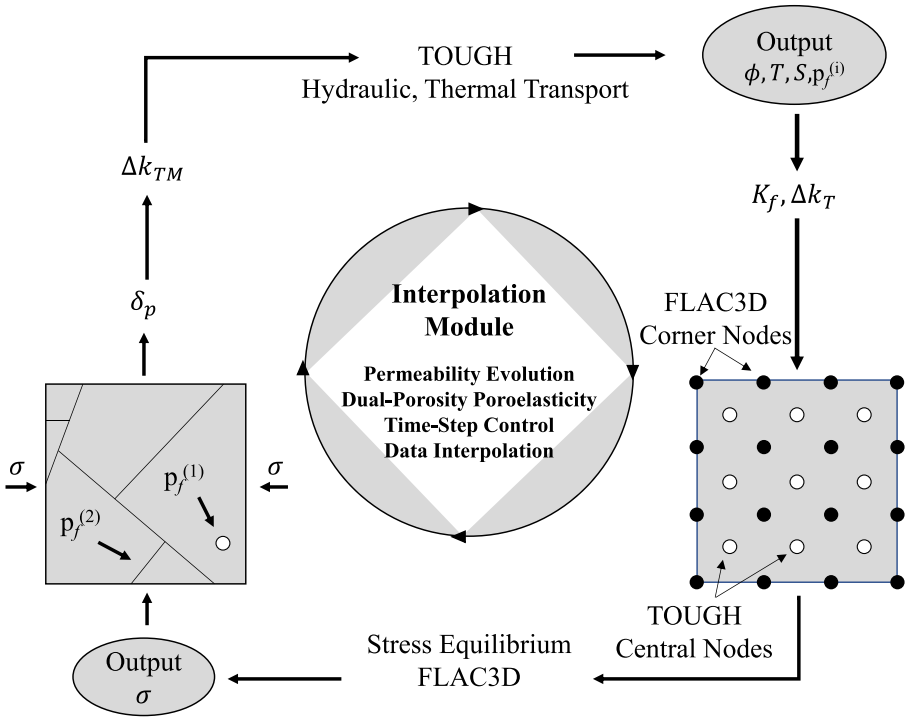

Fig. 1. TOUGH-FLAC3D model simulation coupling procedure.[45]

2.2. Model description

The Pohang EGS, located within the Pohang Basin, was intended to extract geothermal energy from a ~4 km-deep granodioritic reservoir. As mentioned earlier, seismicity relocations have identified the existence of an inclined fault between PX-1 and PX-2 and a smaller fault near PX-1. Thus, we study THM coupled processes in a geothermal reservoir with a major fault (F1) adjacent to a non-intersecting minor fault (F2) during fluid injection and circulation. A pseudo 3D model is built. There are two faults in the reservoir with their location and architecture defined according to the EGS reservoir at Pohang. The fault structure in our model is consistent with the model in Yeo's article.[44] They obtained the best-fit model using hydraulic diffusivities and wellhead pressure data as input. The dip angles of the two fault planes are inferred from observations of seismicity as 43° (F1) and 62° (F2).[49] The larger fault (F1) is located between 3500 m and 4500 m below the ground surface and consists of a 10 m-thick low-permeability fault core, bounded on both sides by an 85 m-thick high-permeability damage zone (Fig. 2b). The fault core is of low permeability, while the damage zone serves as a permeable channel for fluid migration in the direction parallel to the fault strike. The smaller fault (F2) is a 130 m-thick high-permeability fault located at a depth between 3700 m and 4100 m. The minimum separation between F2 and F1 is 10 m at the base of F2 (see Fig. 2a, inset). To ensure the pore pressure and temperature changes do not reach the model boundaries, the model is contained within a rectangular domain of dimensions 3000 m × 2000 m in the x and z directions, respectively. Considering the computational efficiency and the preliminary nature of our study, we chose a pseudo 3D model. The length of the model in the y direction is 15 m, as shown in Fig. 2a. 3D faults exhibit varying dip angles, strike changes, and fault surface curvatures, all of which can affect fault slip behavior and stress distribution. These 3D geometric features may lead to variations in stress concentration zones, thereby influencing the prediction of induced seismic slip. Our model represents a critically-stressed reverse stress state. Under this stress regime, the slip direction and stress changes predominantly occur in the XZ plane. Therefore, while the intricate 3D fault geometry may affect localized stress distribution, our model is capable of capturing the key slip characteristics and stress variations, providing valuable insights.

Based on measurements made during and after drilling PX-2, the initial in-situ stress conditions between depths of 3.4–4.3 km are assumed to be those of reverse faulting. Thus σ_{Hmax} (maximum horizontal compressive stress)>σ_{hmin} (minimum horizontal compressive

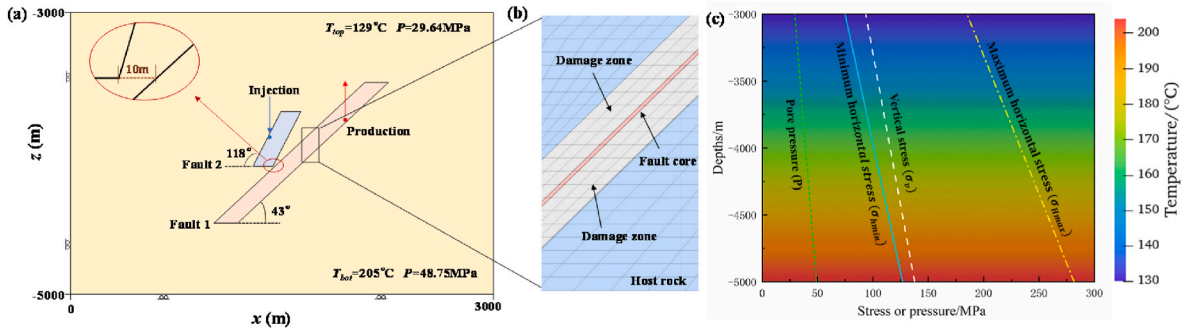

Fig. 2. (a) Schematic of the model domain with the location of injection and production wells indicated. (b) Architecture of the major fault F1. (c) Distributions of the maximum horizontal stress, minimum horizontal stress, vertical stress, pore pressure, and temperature with depth.

stress) $>\sigma_v$ (vertical stress), and the values for these stress components for the Pohang EGS reservoir at 4.2 km depth are 243 MPa, 120 MPa, and 106 MPa, respectively.[49] According to the summary report on the Pohang earthquake,[49] the σ_{Hmax} orientation is reported as 077 ± 23°. Consequently, in our model, the direction of the minimum horizontal principal stress is obtained by rotating the X-axis clockwise by 77°, while the direction of the maximum horizontal principal stress is obtained by rotating the X-axis counterclockwise by 13°. Gradients of the maximum horizontal stress, minimum horizontal stress, and vertical stress are 48.3 MPa/km, 22.1 MPa/km, and 26 MPa/km, respectively.[32] Pore pressures are hydrostatic, rising from 29.64 MPa at 3000 m depth to 48.75 MPa at 5000 m depth. The reservoir temperature at depths of 3 km and 5 km are 129 °C and 205 °C, respectively, with a temperature gradient of 38 °C/km.[50] Fig. 2c shows the distribution of in-situ stresses, pore pressure, and temperature with depth. Roller conditions are imposed on the lower and left boundaries. A constant vertical stress is imposed on the top boundary, and a linearly increasing stress is imposed on the right boundary. There is no fluid flow or heat transfer across all external boundaries.

The key parameters used in the simulation approach are listed in Table 1[51] A bilinear strain-softening ubiquitous-joint model is used to represent the elastic-plastic behavior of the faults, with a plane of weakness set along the orientation of each fault. A strain-softening relationship is adopted by reducing the friction angle with the accumulation of plastic shear strain. For simplicity, we assume a uniform Poisson's ratio of 0.21 and a uniform density of 2630 kg/m^3. The thermal expansion coefficient, specific heat capacity, and thermal conductivity are set uniformly as 1.7×10^{-5} (1/K), 0.799 kJ/(kg·K), and 3.02 W/(m·K), respectively, based on thermal properties derived from laboratory tests.[51] The bulk modulus and shear modulus of the host rock are calculated according to the elastic modulus and Poisson's ratio obtained from laboratory tests. We choose a bulk modulus and shear modulus for the fault to be 9.6 GPa and 6.9 GPa, respectively, which are half the value for the host rock.[14] The initial hydraulic diffusivity of the fault core, fault damage zone, and host rock are applied as 10^{-6} m^2/s, 0.1 m^2/s, and 10^{-8} m^2/s, respectively.[44]

Fig. 3a shows the initial stresses along the two faults. The effective normal stress and shear stress along the two faults both increase linearly with depth. The Coulomb stress ratio, defined as the ratio of the shear stress to the effective normal stress, as shown in Eq. (1), may be applied to evaluate the evolution of the stress state and identify when the fault approaches instability by comparing it against the friction coefficient.[23] The initial Coulomb stress ratios for F1 and F2 decrease linearly with depth.

Table 1
Key parameters used in the simulation approach.

Parameters	Fault	Host rock
Poisson ratio	0.21	0.21
Rock density (kg/m^3)	2630	2630
Thermal expansion coefficient/ (1/K)	1.7×10^{-5}	1.7×10^{-5}
Specific heat capacity (kJ/kgK)	0.799	0.799
Thermal conductivity (W/mK)	3.02	3.02
Bulk modulus (GPa)	9.6	19.25
Shear modulus (GPa)	6.9	13.84
Dilation angle (°)	5.3	–
Tensile Strength (MPa)	0.04	9.2
Initial permeability (m^2)	3.0×10^{-18} (core), 3.0×10^{-13} (damage)	1.5×10^{-15}
Joints spacing (m)	2(core), 0.3(damage)	–
Initial aperture (m)	4.16×10^{-6} (core), 1.02×10^{-4} (damage)	–
Porosity	0.3(core), 0.01(damage)	0.1
Cohesion (MPa)	0	15.2
Friction angle (°)	32 (F1) 20 (F2)	60.2

$$\eta = \frac{\tau_\alpha}{\sigma_{n\alpha} - p} \tag{1}$$

where η is the Coulomb stress ratio, τ_α is the shear stress (MPa), $\sigma_{n\alpha}$ is the normal stress (MPa), and p is the pore pressure (MPa).

The friction coefficients of the cuttings from PX-2 are in the range of 0.54–0.68, with an average of 0.63, determined from cuttings at a depth of 3607 m in PX-2. These are consistent with analogous lithologies sampled in nearby fault outcrops.[49] Thus, the friction angle is set to 32° for F1. The initial Coulomb stress ratio for F1 ranges from 0.524 to 0.548, and the initial Coulomb stress ratio for F2 ranges from 0.331 to 0.336, indicating that F2 is more stable than F1 under initial stress conditions. Farkas et al. found that the friction coefficient for F2 should be lower than that for F1 to match the pressure change when F2 shears during the actural hydraulic stimulation process.[37] Thus, the friction angle is set to 20° for F2. The lower friction angle of F2 may be explained by the presence of chlorite gouge and clayey infilling, as observed in the cuttings.[49,52,53] Fig. 3b illustrates the effective normal stress and shear stress acting on F1 and F2 at a depth of 4000 m.

2.3. Fault permeability

Stress, pressure, and fault slip all have a strong influence on permeability.[23,54] In this study, the evolution of fault permeability during fluid injection is reflected by considering the effects of stress, pressure, and fault slip on fracture aperture. The representation of the permeability is achieved by prescribing the aperture and spacing of joints in the fault-normal and fault-parallel directions. The fault permeability is quantified as[55]:

$$k = \frac{b^3}{12s} \tag{2}$$

where k is the fault permeability (m^2), b is the aperture (m), and s is the joints spacing (m).

The effect of stress, pressure, and shear displacement on fracture aperture are considered. The evolution of aperture caused by stress change is calculated as[56]:

$$b_s = b_r + (b_{\max} - b_r)\exp(-\delta(\sigma' - \sigma_0')) \tag{3}$$

where b_s is the joint aperture considering the normal stress effect (m), $b_{\max}$ is the maximum aperture (m) at zero stress, b_r is the residual aperture (m), δ is a constant that defines the non-linear fracture stiffness (1/MPa), σ' is the effective normal stress (MPa), σ_0' is the initial stress normal to the fractures (MPa).

The aperture change induced by shear displacement of fault joints is evaluated as.

$$b_{dila} = u_{js} \tan \varphi_{jd} \tag{4}$$

where b_{dila} is the aperture change (m) due to shear displacement, u_{js} is the joint shear displacement (m), which represents the plastic shear strain increment calculated from FLAC, and φ_{jd} is the dilation angle.

Considering the influence of both normal closure and shear dilation effects, the final expression for calculating the permeability is given by:

$$k = \frac{(b_s + b_{dila})^3}{12} \tag{5}$$

The aperture change is calculated in interpolation module based on the stress field, following the procedures outlined in Equations (3) and (4). Specifically, these equations describe the relationship between stress changes and aperture variations. Once the aperture change is determined, the permeability is calculated using Equation (5). This updated permeability is then input into TOUGH for the subsequent simulation steps.

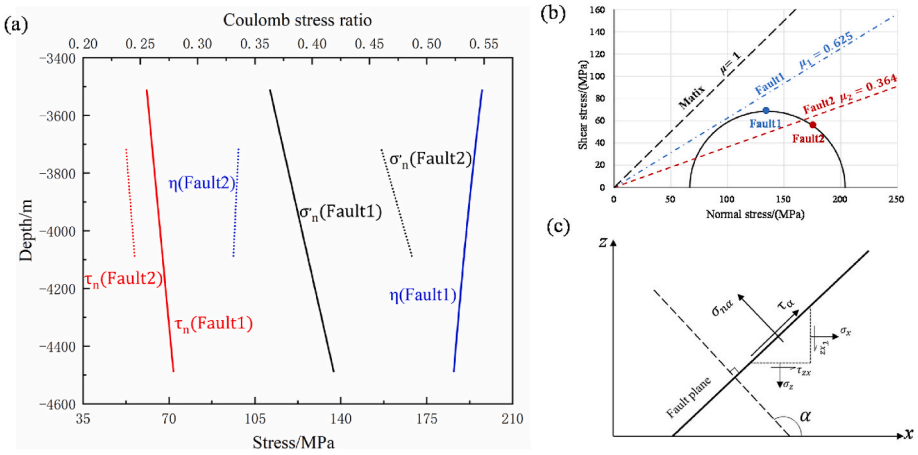

Fig. 3. (a) Initial stress profiles (effective normal stress σ_n', shear stress τ_n) and Coulomb stress ratio (η) distribution along F1 and F2. (b) Mohr-Coulomb failure plot for F1 (blue filled circle) and F2 (red filled circle) at 4 km depth. Two different friction coefficients are assumed for F1 and F2: $\mu_1 = 0.625$ and $\mu_2 = 0.364$. (c) Schematic illustration of fault plane stress analysis. (For interpretation of the references to colour in this figure legend, the reader is referred to the Web version of this article.)

2.4. Fault slip analysis

Whether the fault will slip or not may be evaluated by comparing the shear strength and shear stress on the fault plane. Based on the Coulomb failure criterion, the shear strength is calculated as

$$\tau = c + \mu_s(\sigma_n - p) \tag{6}$$

where τ is the shear strength (MPa), c is the cohesion (MPa), μ_s is the friction coefficient, p is the fluid pressure (MPa), and σ_n is the normal stress acting on the fault (MPa). The normal stresses and shear stresses along the fault are defined as

$$\sigma_{n\alpha} = \frac{\sigma_x + \sigma_z}{2} + \frac{\sigma_x - \sigma_z}{2}\cos 2\,\alpha - \tau_{xz}\sin 2\,\alpha \tag{7}$$

$$\tau_\alpha = \frac{\sigma_x - \sigma_z}{2}\sin 2\alpha + \tau_{xz}\cos 2\,\alpha \tag{8}$$

where α is the angle between the normal to the fault plane and the positive direction of the x-axis (Fig. 2c).

Coulomb failure stress changes (ΔCFS) may be used to describe changes in the stress field around the fault caused by the action of pore pressure diffusion, poroelastic stress changes, and thermal stress - all of which occur simultaneously with the injection of cold fluid.[57] Positive Coulomb failure stress changes suggest a destabilizing stress path, whereas negative Coulomb failure stress changes indicate stabilization. Combining the changes in pore pressure, normal stress, and shear stress on the fault plane, the Coulomb failure stress changes are evaluated as

$$\Delta CFS = \Delta\tau_\alpha - \mu_s\Delta\sigma_{n\alpha} + \mu_s\Delta p \tag{9}$$

where $\Delta\tau_\alpha$ is the change in shear stress on the fault (MPa), $\Delta\sigma_{n\alpha}$ is the change in normal stress on the fault (MPa), and Δp is the pore pressure change in the fault (MPa).

The earthquake moment magnitude, M_w, is estimated as[58,59]:

$$M_w = \frac{\log_{10}M_0}{1.5} - 6.07 \tag{10}$$

$$M_0 = GAd_{avg} \tag{11}$$

where M_0 is the scalar seismic moment (N m), G is the shear modulus of the fault (Pa), A is the rupture area (m^2) which is calculated by assuming a circular rupture patch with the rupture length, and d_{avg} is the average fault slip distance (m) which is obtained by averaging the slip distance of each monitoring point.

2.5. Modeling scenarios

We simulate four scenarios to investigate the evolution of the stress, pressure, and slip potential of the faults under different operational configurations (Table 2). In Scenarios 1 and 2, cold water is directly injected into the center of the damage zone of F2 at a depth of 3887.5 m, at a constant rate of 5 kg/s and a constant injection specific enthalpy of 1.19×10^5 J/kg, to simulate fault response during hydraulic stimulation without the production well. To study the thermal effect caused by cold fluid injection on fault stability, Scenarios 1 is non-isothermal and Scenario 2 is assumed isothermal and therefore neglects thermal effects. Scenarios 3 and 4 are designed to designed to study the stability of the two faults in response to fluid circulation during the long-term operation of the EGS system after hydraulic stimulation. The permeability in the zone connecting the base of F2 and F1 is 6.4 times that of Scenarios 1 and 2, based on the observation that the transmissivity of PX-1 permanently increased by 6.4 times during the stimulation.[36] The production well intersects the F1 damage zone at a depth of 3762.5 m, and the bottom hole pressure of the production well is maintained at 30 MPa from the beginning. Scenarios 3 and 4 are again non-isothermal and isothermal, respectively. Scenarios 1 and 2 are modelled for a duration of one year, while Scenarios 3 and 4 are simulated over ten years. Although this work adopts the Pohang EGS site as a reference for similar fault geometries and rock properties, we emphasize that our goal is not to derive a fully calibrated and validated model of the Pohang EGS. The injection schemes in this study do not match the field conditions. At the Pohang EGS site, a total of five hydraulic stimulation were conducted alternately in two boreholes, PX-1 and PX-2, from 2016 to 2017.

3. Results

The effects of thermal stress and the presence of the extraction well on the stability of the two faults are analyzed by comparing the results of different scenarios in terms of the evolution of pore pressure,

Table 2
Modeling scenarios.

Properties	Scenario 1	Scenario 2	Scenario 3	Scenario 4
Well layout	Injection only	Injection only	Injection-Extraction	Injection-Extraction
Coupling	T-H-M	H-M	T-H-M	H-M
Simulation time	1y	1y	10y	10y

temperature, and Coulomb stress ratio over time. Except for isothermal Scenario 4, faults F1 and F2 slipped in all other scenarios. The slip displacement distributions along the two faults are used to estimate the moment magnitude. The slip time (when the slip occurs), average fault slip displacement, and estimated moment magnitude are summarized in Table 3. In Scenario 1, F1 slips at 41.20 days with a total injected amount of 17,798,040 kg. In Scenario 2, F1 slips at 40.97 days with a total injected amount of 17,699,040 kg.

3.1. Pore pressure and temperature evolution

Fig. 4a and b illustrate the pore pressure increase and rock temperature decrease in the faults and surrounding rocks for non-isothermal Scenario 1 and 3 at two different times, corresponding to the slip times of the two faults. Pore pressure rapidly diffuses along F2 initially due to its highly permeable structure, then extends to F1. Due to the low permeability of the fault core in F1, the pore pressure on the left side of F1 increases faster than that on the right. The injection of cold water initially recovers heat from around the injection well, cooling down the region and forming a low-temperature zone (Fig. 4b). This zone grows and migrates downward. Compared to the diffusion of pore pressure, the expansion of the cooled zone in the reservoir is moderate. Fig. 4c shows the pore pressure and permeability evolution over time at the injection location for the different scenarios. Fig. 4d illustrates the rock temperature evolution at different locations along the faults for non-isothermal Scenarios 1 and 3. As shown in Fig. 4c, at the injection location, pore pressure increases from 38.1 MPa to 78.4 MPa, and rock temperature near the injector decreases from 168 °C to 11 °C after one-year of injection in Scenario 1. Whether or not the thermal effect is considered, the evolution of pore pressure at the injection location shows the same characteristics, indicating that the slips in Scenarios 1 and 2 are dominated by hydro-mechanical effects. The pore pressure at the injection location increases with continuous fluid injection but shows a sudden drop as F2 slips (enlarged area in Fig. 4c). When F1 slips, the pore pressure shows a greater drop, indicating that the slip of F1 impacts F2 and causes a sudden drop in pore pressure. In Scenario 1, at the instant F2 slips, due to shear dilation effects, the permeability at the injection location shows a sudden increase.

Compared to Scenario 1, the evolution of the pore pressure distribution presents different characteristics in Scenario 3. Pore pressure almost stabilizes from the beginning of water circulation due to the presence of a high permeability channel between the production and injection wells. As shown in Fig. 4c, the pore pressure at the injection point only increases from 38.1 MPa to 41 MPa before the slip of F1. Compared with the non-isothermal stimulation injection of Scenario 1, the cooling front advances much further in Scenario 3. As illustrated in Fig. 4d, the rock temperature at B_5 starts to decline sharply at 208 d in Scenario 3, while it does not drop during the entire fluid injection period in Scenario 1. During the evolution of rock temperature at B_5, there is a sudden rise in rock temperature at the time F1 slips (935.19 d), from 73.0 °C to 77.2 °C, as shown in the enlarged area in Fig. 4d. In Scenario 1, there is also an increase in rock temperature when F1 slips (41.20d). This can be explained by the increase in permeability caused by fault slip, which allows the inflow of fluids with higher temperature from depth. In Scenario 1, the temperature at B_5 also shows a sudden rise when F1 slips. Additionally, the rock temperature at the production location starts to drop at 792.82 d, and decreases from 176 °C to 30 °C after ten years of injecting cold water. As shown in Fig. 4c, the evolution of pore pressure at the injection location presents different patterns, suggesting that the slip in Scenario 3 is dominated by stress change due to thermal effects. By comparing the pore pressure and rock temperature distributions in Scenarios 1 and 3, it is apparent that pore pressure significantly influences the stress state of the two faults when the production well is absent (Scenario 1), whereas thermal stress has a major impact on the stress state of the two faults for Scenario 3.

3.2. Coulomb stress ratio evolution

The variation of pore pressure and rock temperature disturbs the effective normal stress and shear stress on the fault plane. In addition to the injection and production locations, six monitoring points along F2 (A_1~A_6) and eleven monitoring points along F1 (B_1~B_{11}) are set in this study (Fig. 4e). The evolution of the Coulomb stress ratio at the monitoring points on F1 and F2 (A_6, injection location, B_5, and B_8) in Scenario 1 is shown in Fig. 5a. With the injection of cold water, the Coulomb stress ratio at A_6 and the injection point on F2 both increase, but the increase is faster at the injection point. Then, the Coulomb stress ratio at the injection point drops sharply at 8.38 d, indicating that the shear stress exceeds the shear strength and triggers fault slip. The contour of plastic strains in F1 and F2 indicates that plastic strain has occurred in the area near the injection point at this time. Seismic rupture propagating from the injector significantly influences the stress state on other fault segments. As shown in Fig. 5a, the Coulomb stress ratio at A_6 along F2 decreases suddenly following the onset of fault reactivation. However, slip on F2 has different effects on different positions of F1, as the Coulomb stress ratio at different positions on F1 evolves with varying magnitudes with slip on F2.

With continuing cold-water injection, more fluids flow into F1. At 41.2 d, the Coulomb stress ratio at B_5 and B_8 of F1 both suddenly decrease, indicating the occurrence of fault slip. The contour of on-fault plastic strain is concentrated in the left zone of F1 at 41.2 d. Slip on F1 impacts the stress state on F2. Later, the Coulomb stress ratio at A_6 rises slightly, but at 202.55 d, it suddenly drops. The failure patterns of the two faults are different. F1 exhibits a global slip over a very short time, while F2 experiences local slips distributed over time. Fig. 5b illustrates the slip displacement distribution on F2 at 8.38 d and the F1 slip distribution at 41.20 d. The maximum slip occurs at the injection point on F2 at the top of F1. Assuming a circular rupture, the moment magnitude for the induced earthquake caused by the slip of F2 and F1 in Scenario 1 is estimated as $M_w = 2.87$ and $M_w = 4.44$, respectively.

Unlike Scenario 1, we use an isothermal condition in Scenario 2 to eliminate the influence of thermal stress. Fig. 5c presents the evolution of the Coulomb stress ratio at monitoring points in F1 and F2 (A_6, injection location, B_5, and B_8) for Scenario 2. The disturbance due to the pore pressure also causes F2 and F1 to slip at 22.34 d and 40.97 d, respectively. Compared to Scenario 1, the time of slip on F2 is delayed by 13.96 d, while no significant impact on the slip timing of F1 is observed. The induced thermal stress extends the time interval between successive slips on F1 and F2. The plastic strain distribution at the times when F1 slips in Scenarios 1 and 2 shows similar characteristics. However, different from Scenario 1, the Coulomb stress ratio rises fastest at A_6, and the rupture initiation position is located in the upper section of F2, as shown in the contours of plastic strain for F1 and F2 at 22.34 d (Fig. 5c). In Scenario 1, the initial position of the rupture is located at the injection

Table 3
Slip time and size of the induced earthquakes.

Scenario	Slip time (d)		d_{avg} (cm)		M_0(N·m)		M_w	
	Fault 2	Fault 1	Fault 2	Fault 1	Fault 2	Fault 1	Fault 2	Fault 1
1	8.38	41.20	2.21	46.58	2.45 E+13	5.42 E+15	2.87	4.44
2	22.34	40.97	1.15	41.32	1.28 E+13	4.81 E+15	2.69	4.41
3	9.25	935.19	1.49	25.75	1.66 E+13	3.00 E+15	2.76	4.27

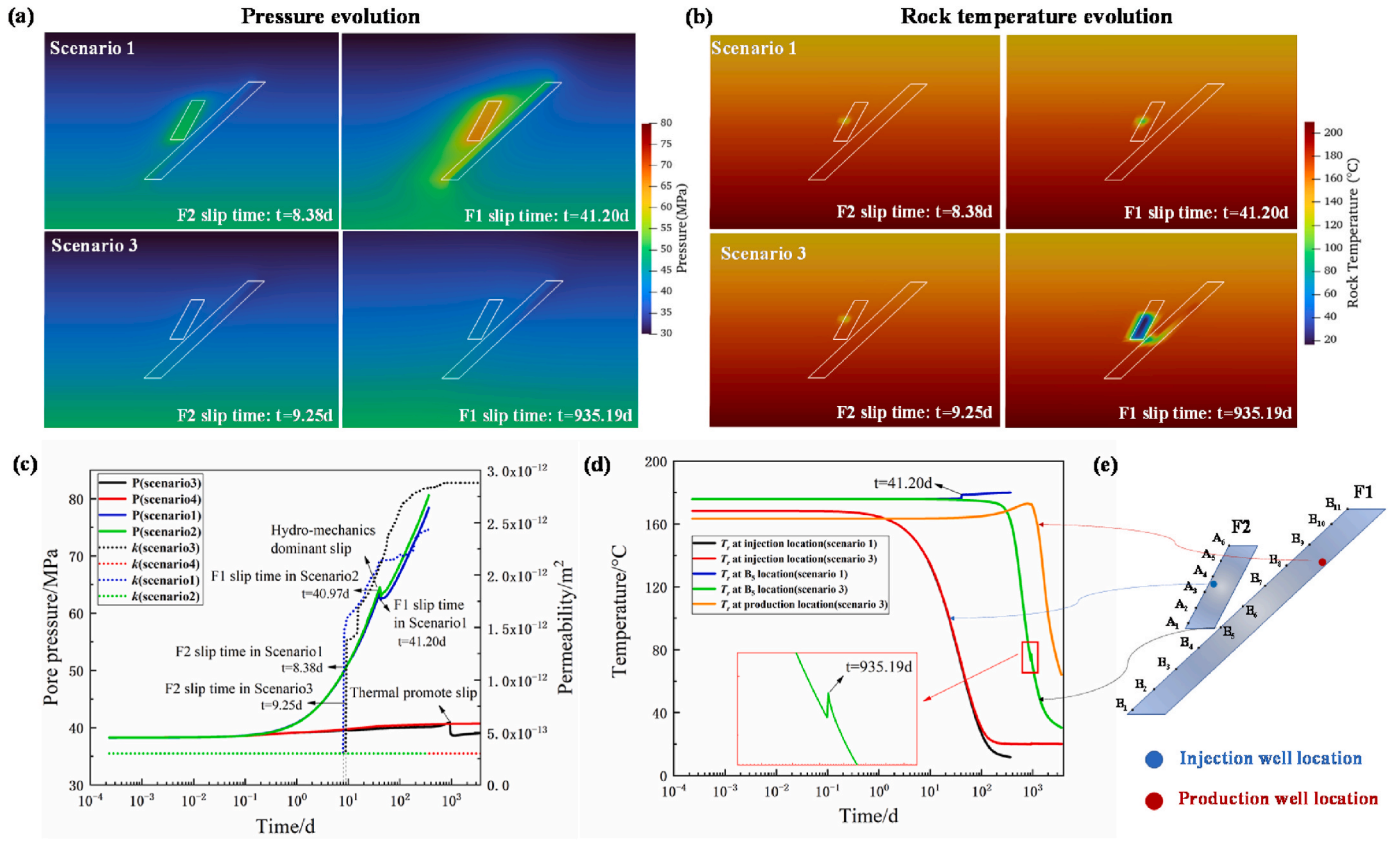

Fig. 4. Pressure and temperature evolution. (a) Pore pressure distributions at different times for Scenarios 1 and 3. (b) Rock temperature distributions at different times for Scenarios 1 and 3. (c) Pore pressure and permeability evolution over time at the injection location for different scenarios. (d) Rock temperature evolution with time at injection, production and B_5 (monitoring point closest to F2 in F1) locations for Scenarios 1 and 3. (e) Locations of the injection well, production well, and different monitoring points in this study.

point. The rock temperature near the injection point drops fastest in Scenario 1, and the thermal stress at the injection point is also the largest, causing the initial rupture position in F2 to occur at the injection point. The permeable channel in the fault damage zone (~300 mD) in Scenario 2 leads to a relatively uniform pressure distribution along the fault dip, causing fault failure to initiate from the upper part of the fault (Fig. 5c). Fig. 5d illustrates the fault slip magnitude at the time of slip. The average slip displacement on F2 and F1 is 1.15 cm and 41.32 cm, respectively. According to equations (10) and (11), the moment magnitudes for the induced earthquakes caused by these slips on F2 and F1 in Scenario 2 are estimated to be $M_w = 2.69$ and $M_w = 4.41$, respectively. A comparison between Scenarios 1 and 2 indicates that thermal stress tends to promote the early onset of fault instability by advancing the timing and translating the rupture point from the upper part of the fault to the injection location.

The Evolution of the Coulomb stress ratio at monitoring points in F1 and F2 (A_6, injection location, B_5, and B_8) in Scenario 3 is given in Fig. 5e. Similar to Scenario 1, the Coulomb stress ratio decreases suddenly at the injection point first among all the monitoring points, but its occurrence at 9.25 d is later than in Scenario 1. Slip on F1 occurs at 935.19 d, which is 2.5 years later than slip on F1 in Scenario 1. At 935.19 d, the distribution of plastic strain on F1 coincides with the area where rock temperature declines (Figs. 5e and 4b). Fig. 5f illustrates the distribution of slip displacement on F2 at 9.25 d and on F1 at 935.19 d. The average slip displacements on F2 and F1 are 1.49 cm and 25.75 cm, respectively, which are smaller than those in Scenario 1. Similarly, the moment magnitudes for the induced earthquake caused by slip on F2 and F1 in Scenario 3 are estimated to be $M_w = 2.76$ and $M_w = 4.27$, respectively. By comparing the slip displacement distribution for the two faults for Scenarios 1 and 3, it is found that the slip displacement is generally of a lower magnitude in Scenario 3. This is mainly due to the addition of a production well in Scenario 3. The production process reduces stress accumulation in the reservoir. Strain energy is released through fluid extraction, resulting in lower slip under the influence of the thermal stress at late time.

Except for considering the influence of temperature, the other parameters in Scenario 4 are identical to those in Scenario 3. However, no slip is detected on F1 and F2 during the 10-year duration of water injection in Scenario 4. In Scenario 4, permeability remains constant at the initial value of 3.0×10^{-13} m^2, whereas in Scenario 3, permeability experiences a slight increases attributed to thermal stress. This elevation in permeability lead to a slightly lower pore pressure compared to Scenario 4. However, the difference in pore pressure between the two scenarios remains within 1 MPa. After slip on F2, triggered by the increase of permeability caused by shear dilation, the pore pressure at the injection location in Scenario 3 is slightly lower than that in Scenario 4. During the entire 10-year injection period, the pore pressure at the injection point increases only slightly, from 38.1 MPa to 40.7 MPa. The small increase in pore pressure, the consistency of the plastic strain area with the area where rock temperature is reduced, together with the simulation result of no fault slip under isothermal conditions all indicate that the fault slip in Scenario 3 is mainly induced by the thermal perturbation.

4. Discussion

4.1. Effect of thermal stress on fault stability

As previously mentioned, the operational results of the models under isothermal and non-isothermal conditions exhibit different

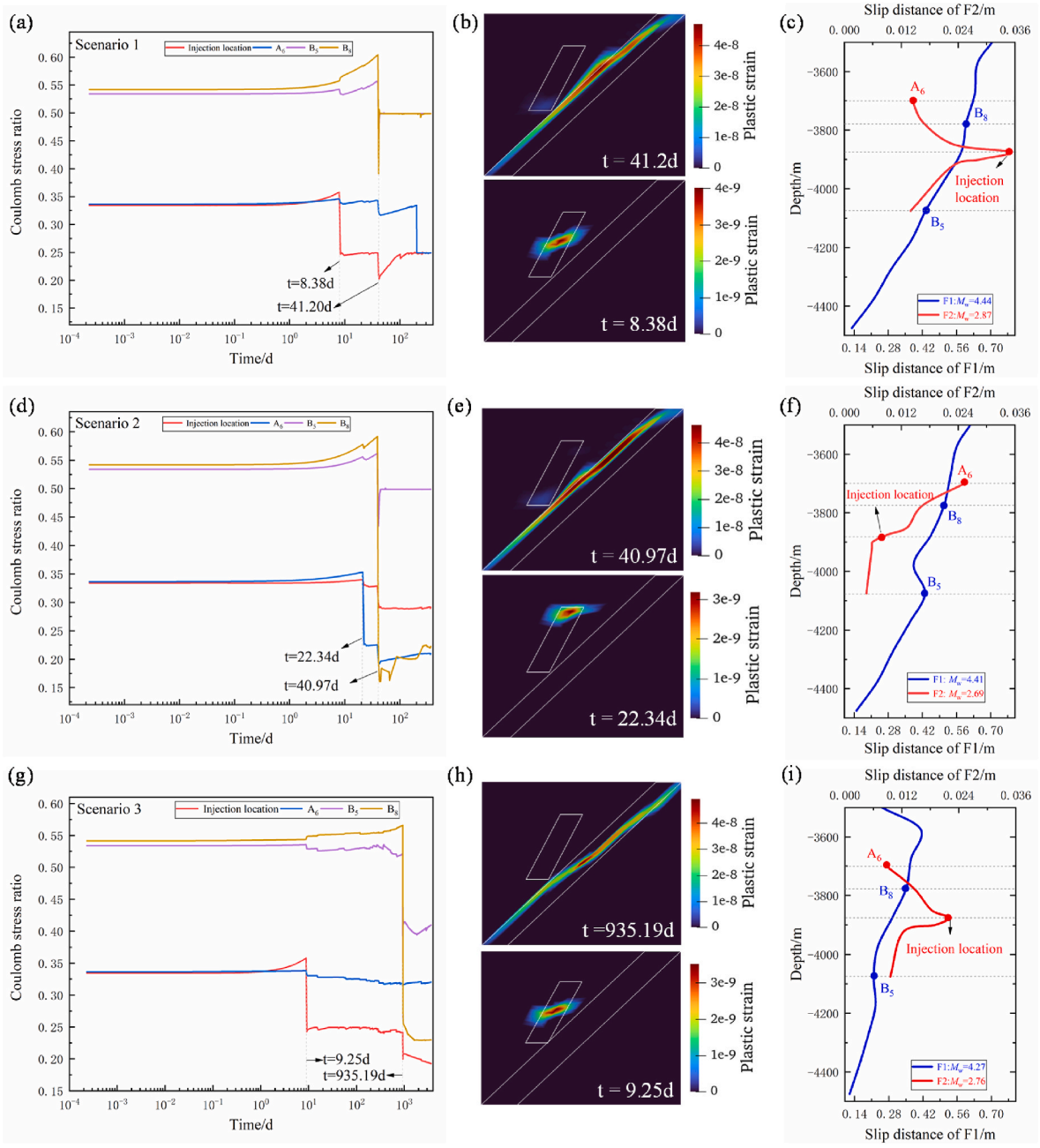

Fig. 5. Evolution of the Coulomb stress ratio at different monitoring points of F1 and F2: (a) Scenario 1; (d) Scenario 2; (g) Scenario 3. The contour of plastic strain of F1 and F2 when the faults slip: (b) Scenario 1; (e) Scenario 2; (h) Scenario 3. Slip distance distribution along F1 and F2: (c) Scenario 1; (f) Scenario 2; (i) Scenario 3.

characteristics, suggesting that thermal stress significantly influences fault reactivation. In this section, the effect of thermal stress on the stability of the two faults is discussed in detail by comparing THM simulation results with HM simulation results.

Fig. 6 provides a detailed comparison of the evolution of pore pressure, rock temperature, effective normal stress, and shear stress for the non-isothermal Scenario 1 and the isothermal Scenario 2 at the injection point on F2 and monitoring point B_5 on F1. Before 0.21 d, the rock temperature at the injection point is maintained at 168 °C for both Scenarios. After 0.21 d, the rock temperature for Scenario 1 begins to decrease, resulting in an increasing difference between the two scenarios. In terms of the pore pressure evolution, the two curves for both scenarios coincide closely before the occurrence of fault slip. Before 0.21 d, the effective normal stress at the injection point on F2 declines extremely slowly from 161.51 MPa to 161.07 MPa under both isothermal and non-isothermal conditions, with the two curves overlapping. After 0.21 d, the effective normal stress decreases more significantly due to the rapid increase of pore pressure. Meanwhile, the kick-in of induced thermal stress lead to a divergence between the two curves, with the effective normal stress decreasing faster for the non-isothermal model. For the non-isothermal Scenario 1, the shear stress at the injection point drops twice when F2 and F1 slip, whereas for the case of isothermal Scenario 2, a significant stress drop occurs only when F1 slips. For B_5 on F1, the evolution of effective normal stress and shear stress for both scenarios is nearly identical, indicating that the involvement of the thermal stress has little effect on the stress state of F1. This is because the thermal front in the reservoir has not reached the major F1 before F1 slips (Fig. 4b).

Fig. 7 compares the pore pressure, rock temperature, effective normal stress, and shear stress under isothermal and non-isothermal

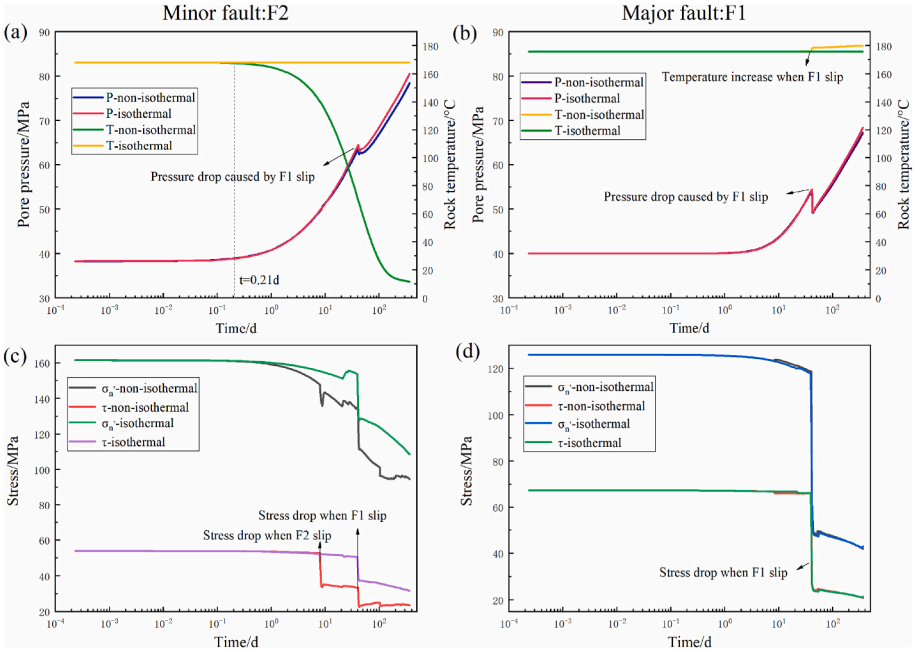

Fig. 6. Comparison of pore pressure and rock temperature under isothermal and non-isothermal conditions at the injection point on F2 (a) and at monitoring point B_5 on F1 (b) for the injection only scenarios (Scenarios 1 and 2). Comparison of effective normal stress and shear stress under isothermal and non-isothermal conditions at the injection point on F2 (c) and at monitoring point B_5 on F1 (d) for the injection only scenarios (Scenarios 1 and 2).

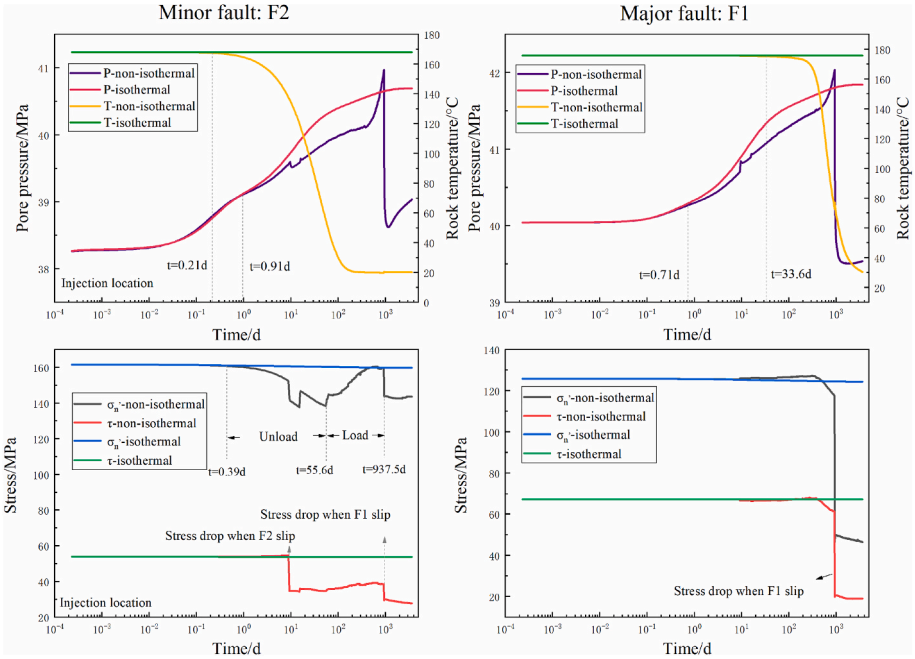

Fig. 7. Comparison of pore pressure and rock temperature under isothermal and non-isothermal conditions at the injection location on F2 (a) and B_5 location on F1 (b) for the injection and extraction scenarios (Scenarios 3 and 4). Comparison of effective normal stress and shear stress under isothermal and non-isothermal conditions at the injection location on F2 (c) and B_5 location on F1 (d) for the injection and extraction scenarios (Scenarios 3 and 4).

conditions at the injector on F2 and monitoring point B_5 on F1 in the injection-extraction scenarios (Scenarios 3 and 4). Unlike the injection-only scenarios, fluid extraction in these scenarios mutes the influence of pore pressure surges, while highlighting the importance of thermal front propagation on the long-term stability of major fault F1 (Fig. 4b). Under Scenario 3, the rock temperature at the injector and F1 starts to drop at 0.21 d and 33.6 d, respectively. The rate of pore pressure increase for non-isothermal Scenario 3 is slower than that for isothermal Scenario 4. Injecting cold fluid causes rock stresses to unload, tending to widen the fracture aperture, thus increasing its permeability.[60] The effective normal stress profile at the injector for non-isothermal Scenario 3 shows a V-shape, indicating the evolution from a loading to an unloading stress state due to the thermal front progression. The decreasing gradient of effective normal stress is enhanced under non-isothermal condition after 0.39 d in the unloading stage. During this stage, the effective normal stress decreases from 160.86 MPa to 140.85 MPa. After 55.6 d, the effective normal stress gradually increases until F1 slips. Comparing the rock temperature evolution with the effective normal stress evolution, it

can be seen that the unloading stage of effective normal stress corresponds to the rapid decline in rock temperature. As the thermal front propagates away from the injector, the effective normal stress gradually recovers (loading stage). Rapid temperature drops cause pronounced thermal shrinkage stress, resulting in unloading by decreasing effective normal stress. As the thermal front propagate away from the injection location, the recovery of the effective normal stress ensues, thereby strengthening F2.

Compared to the isothermal Scenario 4, the evolution of pore pressure at location B_5 reveals that the reactivation of F1 yields the major drop in pore pressure for the non-isothermal Scenario 3. Moreover, the effective normal stress remains almost constant throughout the entire production life, indicating the stable condition of F1 for the isothermal condition. However, the effective normal stress for F1 increases slightly by 1 MPa after F2 slips under non-isothermal condition. When the rock temperature starts to drop significantly (t = 319.44 d), the effective normal stress rapidly decreases. For both isothermal and non-isothermal conditions, the two evolution curves of shear stress at the injection location overlap before the fault slips. At the B_5 location, the shear stress also decreases rapidly after 935.19 d, corresponding to the instability of F1. Therefore, the induced thermal stress could trigger the instability of nearby F1.

For the injection-only scenarios (Scenario 1 and Scenario 2), the hydro-mechanical influence dominates the cause of fault slip. For Scenario 1, thermal effects accelerate the onset of fault slip. The shear stress along the F2 plane exceeds the fault strength for Scenario 1, primarily due to the decrease of effective normal stress acting on the fault plane caused by combined thermoelastic and poroelastic effects. However, for the injection and extraction scenarios (Scenario 3 and Scenario 4), thermal effects are the main reason for inducing fault slip. This indicates that the thermal stress caused by cold fluid injection could make the nearby critically stressed fault slip, even without a significant increase in pore pressure iduring geothermal exploitation.

4.2. *Effect of stress transfer on fault stability*

As illustrated in Fig. 5, the Coulomb stress ratio at different positions on F1 evolved in varying magnitudes with the slips on F2, indicating that the slip on F2 impacts the stress state and the stability of F1. Meanwhile, at the moment F1 slips, the shear stress at the injection point suddenly

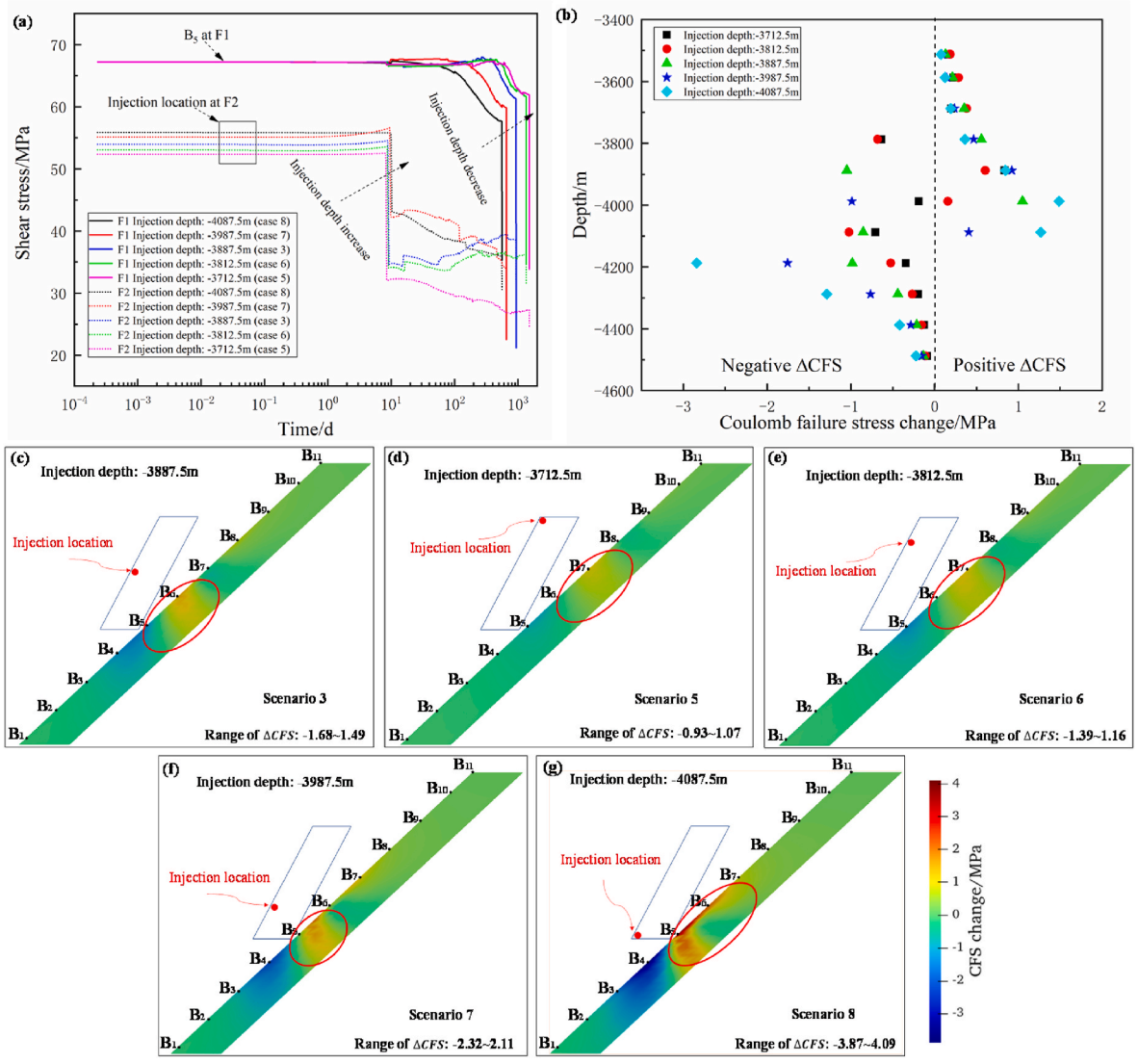

Fig. 8. (a) Evolution of shear stress at injection location on F2 and at B5 location on F1 for different injection depths. (b) Distribution of the Coulomb Failure Stress changes at monitoring locations after F2's slip for different injection depths. (c)–(g) Distribution of the Coulomb Failure Stress changes along F1 after F2's slip for different injection depths. The red ellipses highlight areas with larger positive CFS changes. (For interpretation of the references to colour in this figure legend, the reader is referred to the Web version of this article.)

decreases (Figs. 6c and 7c), indicating that the reactivation of F1 could destabilize F2. This suggests that the slip of either fault affects the stress state of the other fault through stress transfer in a conjugate-faulted geothermal reservoir. In this section, the influence of the slip on F2 on the stress state and stability of F1 is discussed in detail.

The relevance of the perturbations caused by the slip on F2 to the stability of F1can be evaluated by analyzing the change of Coulomb Failure Stress (CFS) on the plane of F1. To understand the stress disturbance caused by the slip on F2 for Scenario 3, the change in CFS along F1 at the moment F2 slips (9.25 d) is evaluated and compared, as shown in Fig. 8c. The CFS change is computed for a plane with a dip of 43°, consistent with the dip of F1. The results show that the larger positive changes in CFS occur near B_6, with an increase of 1.05 MPa. In contrast, the largest negative changes in CFS are observed near B_4 and B_7, with values of −0.98 MPa and −1.05 MPa, respectively. Additionally, the CFS change in the upper part of F1 (>-3787.5 m) exhibits an increasing feature, indicating a destabilizing stress path on the upper fault patch. Conversely, the CFS change in the lower part of F1 (<-4087.5 m) shows a decreasing feature, illustrating a stabilizing stress path on the lower area. In conclusion, the slip on F2 perturbs the stress state of F1, reducing the stability of the upper part while increasing the stability of the lower part.

To identify ways to mitigate or delay the occurrence of fault slip, we investigate the impact of varying injection depth on fault stability. The prescribed simulation scenarios are detailed in Table 4. Injection depth was varied from −4087.5 m to −3712.5 m while maintaining a constant injection flow rate and temperature of 5 kg/s and 20 °C, respectively.

Fig. 8a illustrates the evolution of shear stress at the injection location on F2 and B_5 on F1 for different injection depths. Regardless of the injection depth, F1 and F2 slip successively. However, the difference in injection depth leads to a change in the required time for F1 and F2 reactivation. The slip time for F2 increases with increasing injection depth, while the timing required for F1 reactivation decreases with the increasing injection depth. When the injection depth increases from 3712.5 m to 4087.5 m, the sliding time of F2 is delayed by 1.76 d, while the sliding time of F1 is advanced by 952.55 d. As mentioned earlier, the Coulomb stress ratio decreases linearly with depth (Fig. 3a), indicating that the lower part of F2 is more stable than the upper part. Therefore, when the injection location is set at a deeper depth, a longer injection lead time is required for F2 to slip.

To investigate the reason behind the decrease in slip time of F1 with increasing injection depth, we identify whether there is a difference in the impact of F2 slip on F1 stability when the injection position is at different depths. The CFS changes along F1 between the slip moment of F2 and the previous time step are calculated for different injection depth conditions, as shown in Fig. 8c–g. The CFS changes at the monitoring locations (B_1–B_{11}) for the different injection depths are given in Fig. 8b. The CFS changes for F1 exhibit similar features for different injection depths as F2 slips, with negative changes in the lower part and positive changes in the upper fault patch. However, the degree of Δ *CFS* varies with the injection depth. As the injection depth increases, the range of Δ *CFS* expands from −0.93∼1.07 to −3.87∼4.09. In addition, the area of larger positive Coulomb failure stress changes also shifts downwards along F1 with the increase of injection depth at F2 (red ellipses in Fig. 8c–g). When the injection depth is deeper, the slip on F2 weakens the upper part of F1 more strongly through stress transfer, resulting in an earlier slip time of F1.

In summary, stress transfer created by the slip of F2 reduced the stability of the upper part of F1. The proximity of the injection location (rupture point) to F1 determines the extent of the impact of these stress changes on the stability of F1. Slip on F1 would be delayed by positioning the injection site away from the junction of the two faults. These results emphasize the necessity of evaluating thermal recovery efficiency and fault stability analysis under various injection strategies to ensure the safe and efficient exploitation of geothermal resources. The implications could be useful in guiding field operations in EGS with multiple conjugate but non-intersecting faults.

Table 4
Scenarios with different injection depths.

Scenario	Injection flow rate (kg/s)	Injection specific enthalpy (J/kg)	Injection depth (m)
5	5	1.19×10^5	−3712.5
6	5	1.19×10^5	−3812.5
3	5	1.19×10^5	−3887.5
7	5	1.19×10^5	−3987.5
8	5	1.19×10^5	−4087.5

5. Conclusion

We conducted a systematic study of the influence of fault slip on the stability of an adjacent fault, together with thermal effects, by simulating the injection of the cold fluid into a reservoir with adjacent but non-intersecting conjugate faults (F1 and F2). This geometry is established based on the Pohang EGS project. The evolution of the local distribution of effective stress along the two faults during cold-water injection was investigated to analyze stress transfer and to follow the interaction in instability on the two faults. The results indicate that mechanical and hydrological effects are the main factors triggering fault reactivation in the injection-only scenarios, while the impact of thermal stresses plays a decisive role in causing fault reactivation at relatively later stages in the fluid circulation scenarios.

Except for injection and extraction scenarios without considering the thermal effect (Scenario 4), water injection into F2 successively causes F2 and F1 to slip. In scenarios where the production well is absent, the disturbance by pore pressures causes dominates, with an increase of up to 78.4 MPa. While for injection and extraction scenarios (Scenarios 3 and 4), the increment of pore pressure is limited, as the pore pressure almost stabilizes from the very beginning of water circulation due to the presence of a high permeability channel between the production and injection wells. Compared with Scenarios 1 and 3, fluid extraction delays the slip of F2 by 0.87 d and F1 by 2.5 years, thereby highlighting the impact of heat transfer in modulating fault stability.

Thermal stress is shown to play an important role in triggering slip by reducing effective normal stress along the fault planes and thereby decreasing the shear strength. In injection-only scenarios (Scenario 1 and 2), although mechanical and hydrological effects are the primary reasons for fault reactivation, thermal stresses advance the timing of slip on F2 by 14 d and shifts the rupture point from the upper part of F2 to the injection location. In the long-term fluid injection-extraction scenarios (Scenario 3 and 4), there is no slip in Scenario 4 without considering the thermal effect. However, thermal stress triggers slip in Scenario 3, indicating that thermal stress caused by cold fluid injection could cause local critically stressed faults to slip even without excessive pore pressure increase during later stage geothermal exploitation. Additionally, fault strengthening is observed at the injection location in Scenario 3 as a result of the propagation of the thermal front (Fig. 7c). As the thermal front propagation fades away from the injection location, the effective normal stress along F2 recovers.

The failure sequence patterns for the two faults are different. F1 presents an overall slip in a very short time, while F2 is subject to local slips at different times. Slip on F2 affects the stability of the adjacent major fault, F1. The closer F1 is to the rupture location on F2, the greater the impact of F2 in changing the stress state on F1. Slip on F2 mainly weakens the upper section of F1, while it enhances the stability of the lower section of F1. Conversely, slip on F1 also affects the stability of F2. Slip on F1 disturbs the stress state on F2, resulting in secondary slip on F2. Finally, simulations with varying injection depths are conducted to improve our understanding of how different injection strategies can relieve or delay induced seismicity. Slip on F1 may be delayed by positioning the injection site away from the junction of the two faults.

Reducing the injection depth from 4087.5 m to 3712.5 m could result in a delay of 952.55 d in the time to sliding on F1.

CRediT authorship contribution statement

Yueqiang Ma: Data curation, Funding acquisition, Methodology, Writing – original draft. **Kaiwen Xia:** Writing – review & editing. **Qinghua Lei:** Visualization, Writing – review & editing. **Chongyuan Zhang:** Writing – review & editing. **Derek Elsworth:** Software, Writing – review & editing. **Quan Gan:** Conceptualization, Funding acquisition, Investigation, Resources, Software, Supervision, Writing – review & editing. **Liang Yuan:** Supervision, Writing – review & editing.

Declaration of competing interest

The authors declare that they have no known competing financial interests or personal relationships that could have appeared to influence the work reported in this paper.

Data availability

Data will be made available on request.

Acknowledgements

This study was supported by the National Key Research and Development Program (Grant:2021YFC3000603), the Natural Science Foundation of China (Grant No. 42307201, 5217041034, 42177175), the Fundamental Research Funds for the Central Universities (Project No. 2023CDJKYJH041). DE acknowledges support from the G. Albert Shoemaker endowment.

References

1. Soltani M, Moradi Kashkooli F, Dehghani-Sanij AR, et al. A comprehensive review of geothermal energy evolution and development. *Int J Green Energy*. 2019;16(13):971–1009.
2. Zhang C, Huang R, Qin S, et al. The high-temperature geothermal resources in the Gonghe-Guide area, northeast Tibetan plateau: a comprehensive review. *Geothermics*. 2021;97, 102264.
3. Aghahosseini A, Breyer C. From hot rock to useful energy: a global estimate of enhanced geothermal systems potential. *Appl Energy*. 2020;279, 115769.
4. Majer EL, Baria R, Stark M, et al. Induced seismicity associated with enhanced geothermal systems. *Geothermics*. 2007;36(3):185–222.
5. Grünthal G. Induced seismicity related to geothermal projects versus natural tectonic earthquakes and other types of induced seismic events in Central Europe. *Geothermics*. 2014;52:22–35.
6. Cornet F, Helm J, Poitrenaud H, Etchecopar A. Seismic and aseismic slips induced by large-scale fluid injections. *Pure Appl Geophys*. 1997;150:563–583.
7. Kim Kwang-Hee, Ree Jin-Han, Kim YoungHee, Kim Sungshil, Kang Su Young, Seo W. Assessing whether the 2017 M 5.4 Pohang earthquake in South Korea was an induced event. *Science*. 2018;360(6392):1003–1007.
8. Majer EL, Peterson JE. The impact of injection on seismicity at the Geysers, California Geothermal Field. *Int J Rock Mech Min Sci*. 2007;44(8):1079–1090.
9. Häring MO, Schanz U, Ladner F, Dyer BC. Characterisation of the Basel 1 enhanced geothermal system. *Geothermics*. 2008;37(5):469–495.
10. Rathnaweera TD, Wu W, Ji Y, Gamage RP. Understanding injection-induced seismicity in enhanced geothermal systems: from the coupled thermo-hydro-mechanical-chemical process to anthropogenic earthquake prediction. *Earth Sci Rev*. 2020;205, 103182.
11. Healy JH, W WR, Griggs DT, Raleigh CB. The Denver Earthquakes. *Science*. 1968;161(3848):1301–1310.
12. Konstantinovskaya E, Li Q, Malo M, Rivero JA, Faskhoodi MM, Campbell B. Strike-slip reactivation of a high-angle normal fault induced by increase of reservoir pore pressure: insight from 3D coupled reservoir-geomechanical modeling. *Int J Greenh Gas Control*. 2020;102, 103159.
13. Schultz R, Beroza GC, Ellsworth WL. A risk-based approach for managing hydraulic fracturing-induced seismicity. *Science*. 2021;372:504–507.
14. Zbinden D, Rinaldi AP, Urpi L, Wiemer S. On the physics-based processes behind production-induced seismicity in natural gas fields. *J Geophys Res Solid Earth*. 2017;122(5):3792–3812.
15. Cebry SBL, McLaskey GC. Seismic swarms produced by rapid fluid injection into a low permeability laboratory fault. *Earth Planet Sci Lett*. 2021;557, 116726.
16. Gischig VS, Giardini D, Amann F, et al. Hydraulic stimulation and fluid circulation experiments in underground laboratories: stepping up the scale towards engineered geothermal systems. *Geomechanics for Energy and the Environment*. 2020;24, 100175.
17. Thibault Candela BW, Heege Jan ter, Buijze Loes. *How earthquakes are induced Science*. 2018;360(6389):598–600.
18. Heffer K. Geomechanical influences in water injection projects: an overview. *Oil Gas Sci Technol*. 2006;57(5):415–422.
19. Jacquey AB, Urpi L, Cacace M, Blöcher G, Zimmermann G, Scheck-Wenderoth M. Far field poroelastic response of geothermal reservoirs to hydraulic stimulation treatment: theory and application at the Groß Schönebeck geothermal research facility. *Int J Rock Mech Min Sci*. 2018;110:316–327.
20. Bhattacharya P, Viesca RC. Fluid-induced aseismic fault slip outpaces pore-fluid migration. *Science*. 2019;364(6439):464–468.
21. Gan Q, Elsworth D. Analysis of fluid injection-induced fault reactivation and seismic slip in geothermal reservoirs. *J Geophys Res Solid Earth*. 2014;119(4):3340–3353.
22. Gan Q, Elsworth D. Thermal drawdown and late-stage seismic-slip fault reactivation in enhanced geothermal reservoirs. *J Geophys Res Solid Earth*. 2014;119(12):8936–8949.
23. Gan Q, Lei Q. Induced fault reactivation by thermal perturbation in enhanced geothermal systems. *Geothermics*. 2020;86, 101814.
24. Im K, Avouac J-P. On the role of thermal stress and fluid pressure in triggering seismic and aseismic faulting at the Brawley Geothermal Field, California. *Geothermics*. 2021;97, 102238.
25. Pathikrit Bhattacharya, Viesca RC. Fluid-induced aseismic fault slip outpaces pore-fluid migration. *Science*. 2019;364:464–468.
26. Guglielmi Y, Cappa F, Avouac J-P, Henry P, Elsworth D. Induced seismicity: seismicity triggered by fluid injection-induced aseismic slip. *Science*. 2015;348:464–468.
27. Brown MRM, Ge S. Small earthquakes matter in injection-induced seismicity. *Geophys Res Lett*. 2018;45(11):5445–5453.
28. Cao W, Durucan S, Shi J-Q, Cai W, Korre A, Ratouis T. Induced seismicity associated with geothermal fluids re-injection: poroelastic stressing, thermoelastic stressing, or transient cooling-induced permeability enhancement? *Geothermics*. 2022;102, 102404.
29. Catalli F, Rinaldi AP, Gischig V, Nespoli M, Wiemer S. The importance of earthquake interactions for injection-induced seismicity: retrospective modeling of the Basel Enhanced Geothermal System. *Geophys Res Lett*. 2016;43(10):4992–4999.
30. Burnside NM, Westaway R, Banks D, Zimmermann G, Hofmann H, Boyce AJ. Rapid water-rock interactions evidenced by hydrochemical evolution of flowback fluid during hydraulic stimulation of a deep geothermal borehole in granodiorite: Pohang, Korea. *Appl Geochem*. 2019;111, 104445.
31. Urpi L, Rinaldi AP, Rutqvist J, Wiemer S. Fault stability perturbation by thermal pressurization and stress transfer around a deep geological repository in a clay formation. *J Geophys Res Solid Earth*. 2019;124(8):8506–8518.
32. Wassing BBT, Gan Q, Candela T, Fokker PA. Effects of fault transmissivity on the potential of fault reactivation and induced seismicity: implications for understanding induced seismicity at Pohang EGS. *Geothermics*. 2021;91, 101976.
33. Ellsworth WL, Giardini D, Townend J, Ge S, Shimamoto T. Triggering of the Pohang, Korea, earthquake (Mw 5.5) by enhanced geothermal system stimulation. *Seismol Res Lett*. 2019;90:1844–1858.
34. Woo JU, Kim M, Sheen DH, et al. An in-depth seismological analysis revealing a causal link between the 2017 M_W 5.5 Pohang earthquake and EGS project. *J Geophys Res Solid Earth*. 2019;124(12):13060–13078.
35. GrigoliS FC, Rinaldi AP, Manconi A, et al. The November 2017 M_W 5.5 Pohang earthquake: a possible case of induced seismicity in South Korea. *Science*. 2018;360(6392):1003–1006.
36. Park S, Kim K-I, Xie L, et al. Observations and analyses of the first two hydraulic stimulations in the Pohang geothermal development site, South Korea. *Geothermics*. 2020;88, 101905.
37. Farkas MP, Hofmann H, Zimmermann G, et al. Hydromechanical analysis of the second hydraulic stimulation in well PX-1 at the Pohang fractured geothermal reservoir, South Korea. *Geothermics*. 2021;89, 101990.
38. Yoo H, Park S, Xie L, et al. Hydro-mechanical modeling of the first and second hydraulic stimulations in a fractured geothermal reservoir in Pohang, South Korea. *Geothermics*. 2021;89, 101982.
39. Kim K-I, Yoo H, Park S, et al. Induced and triggered seismicity by immediate stress transfer and delayed fluid migration in a fractured geothermal reservoir at Pohang, South Korea. *Int J Rock Mech Min Sci*. 2022;153, 105098.
40. Chang KW, Yoon H. Mitigating injection-induced seismicity along basement faults by extraction: application to 2016–2018 Pohang earthquakes. *J Geophys Res Solid Earth*. 2021;126(4), e2020JB021486, 126.
41. Shapiro SA, Kim KH, Ree JH. Magnitude and nucleation time of the 2017 Pohang Earthquake point to its predictable artificial triggering. *Nat Commun*. 2021;12(1):6397.
42. Kaown D, Lee KK, Kim J, et al. Earthquakes and very deep groundwater perturbation mutually induced. *Sci Rep*. 2021;11(1), 13632.
43. Westaway R, Burnside NM. Fault “corrosion” by fluid injection: a potential cause of the november 2017 MW 5.5 Korean earthquake. *Geofluids*. 2019;2019:1–23.
44. Yeo IW, Brown MRM, Ge S, Lee KK. Causal mechanism of injection-induced earthquakes through the Mw 5.5 Pohang earthquake case study. *Nat Commun*. 2020;11(1):2614.
45. Taron J, Elsworth D. Thermal–hydrologic–mechanical–chemical processes in the evolution of engineered geothermal reservoirs. *Int J Rock Mech Min Sci*. 2009;46(5):855–864.
46. Im K, Avouac JP, Heimisson ER, Elsworth D. Ridgecrest aftershocks at Coso suppressed by thermal destressing. *Nature*. 2021;595(7865):70–74.
47. Lv Y, Yuan C, Zhu X, Gan Q, Li H. THMD analysis of fluid injection-induced fault reactivation and slip in EGS. *Geothermics*. 2022;99, 102303.

48. Hu Y, Gan Q, Hurst A, Elsworth D. Investigation of coupled hydro-mechanical modelling of hydraulic fracture propagation and interaction with natural fractures. *Int J Rock Mech Min Sci*. 2023;169, 105418.
49. Lee K-K. *Summary Report of the Korean Government Commission on Relations between the 2017 Pohang Earthquake and EGS Project*. Korea: Seoul: The Geological Society of; 2019.
50. Lee TJ, Song Y, Park D-W, Jeon J, Yoon WS. Three dimensional geological model of Pohang EGS pilot site Korea. In: *Proceedings World Geothermal Congress*. 2015. Melbourne, Australia.
51. Kwon S, Xie L, Park S, et al. Characterization of 4.2-km-Deep fractured granodiorite cores from Pohang geothermal reservoir, Korea. *Rock Mech Rock Eng*. 2018;52(3): 771–782.
52. K.K., L.. *Final Report of the Korean Government Commission on Relations between the 2017 Pohang Earthquake and EGS Project*. Korea: The Geological Society of; 2019.
53. Woosangwoo, Kim C-M, Jeong GY, Jeong J, Lee H. Relation between temporal change of fault rock materials and mechanical properties. *J Geol Soc Korea*. 2016;52 (6):847–861.
54. Rutqvist J, Stephansson O. The role of hydromechanical coupling in fractured rock engineering. *Hydrogeol J*. 2003;11(1):7–40.
55. Snow DT. Anisotropic permeability of fractured media. *Water Resour Res*. 1969;5(6): 1273–1289.
56. Rutqvist J, S.W Y, Tsang C-F, Bodvarsson G. A modeling approach for analysis of coupled multiphase fluid flow, heat transfer, and deformation in fractured porous rock. *Int J Rock Mech Min Sci*. 2002;39:429–442.
57. Harris RA. Earthquake stress triggers, stress shadows, and seismic hazard. *Curr Sci*. 2000;79:1215–1225.
58. Hiroo Kanamori DA. Theoretical basis of some empirical relations in seismology. *Bull Seismol Soc Am*. 1975;65(5):1073–1095.
59. Kanamori H, Brodsky EE. The physics of earthquakes. *Rep Prog Phys*. 2004;67(8): 1429–1496.
60. Ghassemi A, Tao Q. Thermo-poroelastic effects on reservoir seismicity and permeability change. *Geothermics*. 2016;63:210–224.